The hydrometeor partitioning and microphysical processes over the Pacific Warm Pool in numerical modeling

Yi-Chih Huang[1] and Pao K. Wang[1,2,a]

[1] Research Center for Environmental Changes, Academia Sinica, Taipei, Taiwan
[2] Department of Atmospheric and Oceanic Sciences, University of Wisconsin-Madison, Madison, Wisconsin, USA

September 2016
Submitted for publication for Atmospheric Research

[a] Corresponding author address: Dr. Pao K. Wang, Research Center for Environmental Changes, Academia Sinica, 128 Academia Road, Section 2, Nankang, Taipei, 115, Taiwan.
Email: pkwang@gate.sinica.edu.tw

Abstract

Numerical modeling is conducted to study the hydrometeor partitioning and microphysical source and sink processes during a quasi-steady state of thunderstorms over the Pacific Warm Pool by utilizing the microphysical model WISCDYMM to simulate selected storm cases. The results show that liquid-phase hydrometeors dominate thunderstorm evolution over the Pacific Warm Pool. The ratio of ice-phase mass to liquid-phase mass is about 41% : 59%, indicating that ice-phase water is not as significant over the Pacific Warm Pool as the liquid water compared to the larger than 50% in the subtropics and ~ 80% in US High Plains in a previous study. Sensitivity tests support the dominance of liquid-phase hydrometeors over the Pacific Warm Pool.

The major rain sources are the key hail sinks: melting of hail and shedding from hail; whereas the crucial rain sinks are evaporation and accretion by hail. The major snow sources are Bergeron-Findeisen process, transfer of cloud ice to snow and accretion of cloud water; whereas the foremost sink of snow is accretion by hail. The essential hail sources are accretions of rain, cloud water, and snow; whereas the critical hail sinks are melting of hail and shedding from hail. The contribution and ranking of sources and sinks of these precipitates are compared with the previous study.

Hydrometeors have their own special microphysical processes in the development and depletion over the Pacific Warm Pool. Microphysical budgets depend on atmospheric dynamical and thermodynamical conditions which determine the partitioning of hydrometeors. This knowledge would benefit the microphysics parameterization in cloud models and cumulus parameterization in global circulation models.

1. Introduction

Poor precipitation performance in general circulation models (GCMs) has been a serious problem in the atmospheric science community. The parameterizations of cloud species have close links to convection and precipitation modeling, which is closely related to radiation and large-scale circulation in GCMs, and thus has large impacts on climate modeling as well. Successful numerical modeling of precipitation in GCMs depends very much on model resolution and cloud parameterization. It was suggested that if the resolution of GCMs can resolve convective systems realistically, the problems on the numerical modeling of precipitation and tropical cyclones will meliorate (Hourdin et al. 2006; Randall et al. 2007).

If the convective cloud parameterization in GCM can include the effect of the Microphysical budget of convective clouds in different geographic zones, the predictions of convective cloud properties in GCM would be greatly improved. The microphysical budgets such as hydrometeor partitioning, microphysical processes, etc. in the quasi-steady state in mature convective storms in the US High Plains and some subtropical locations have been previously investigated by Lin et al. (2005, hereafter LWS05). Their results show that partitioning of hydrometeors in deep convective clouds is sensitive to geographical location. At the present stage, it is impossible to include detailed cloud microphysical processes in a GCM and hence it is useful to parameterize the cloud partitioning in deep convective clouds that take the geographic location into account.

One of the regions of great importance to climate studies is the Pacific Warm Pool (Wang and Xie, 1998; Barlow et al., 2002). The Pacific Warm Pool plays a significant role in global heat and water vapor transport; hence, the understanding of the cloud properties including how hydrometeors are partitioned is of great importance. There has been some research related to the hydrometeor partitioning over the Pacific Warm Pool. Chen and Yin (2011) showed the hydrometeor partitioning in a case study in Darwin using a three-dimensional nonhydrostatic convective cloud model with a double-moment bulk microphysics scheme and explicit droplet activation from cloud condensation nuclei. Based on cloud budget employing a two-dimensional cloud-resolving model and simulation data during TOGA COARE, Li et al. (2011) obtained net condensation and hydrometeor change/convergence. With the simulations triggered by large-scale forcing data, Li and Shen (2013) examined the rain microphysical processes connected with precipitation in the tropical deep convection using a 2-D cloud model. Based on the measurements of the shape and electric charge of hydrometeors by a videosonde, Takahashi (2004) constructed a conceptual model of hydrometeor mass, number, and space charge evolution for convective clouds around Tiwi Islands.

In the above studies, the hydrometeor partitioning was only about a certain sounding, and there is no study of microphysical processes over the Pacific Warm Pool. In this study, we utilize a numerical cloud model to examine the dynamic and thermodynamic fields, and the details of hydrometeors and microphysical processes during the quasi-steady state of some thunderstorms over the Pacific Warm Pool. We also study the differences in hydrometeor partitioning, and microphysical processes among the thunderstorms in the Pacific Warm Pool, subtropics and High Plains in LWS05.

This paper is organized as follows. Section 2 introduces the cloud model employed in this study. Section 3 describes three Pacific Warm Pool storm cases and verifies the numerical simulations by observations. In section 4 we investigate the time evolution of microphysical budgets of them. Section 5 compares the specialties of microphysical budgets in the storms in Pacific Warm Pool with subtropics and High Plains in LWS05. Summary is given in Section 6.

2. Model description

The numerical model used in this study is the Wisconsin Dynamical/Microphysical Model (WISCDYMM), which is a three-dimensional, quasi-compressible, non-hydrostatic primitive-equation cloud model taken from Anderson et al. (1985) (Straka 1989; Johnson et al., 1993; 1995; Wang, 2003). The microphysics of this model is based on those in Lin et al. (1983) and Cotton et al. (1982, 1986). The hydrometeors have six categories: water vapor, cloud water, cloud ice, rain, snow, and graupel/hail. The bulk method is applied to parameterize 38 microphysical processes including autoconversion, nucleation, condensation, accretion, evaporation, freezing, melting, sublimation, deposition, etc. Except for cloud ice which is assumed to be hexagonal plates, hydrometeors are assumed to be spherical. The cloud water is supposed to be monodispersed with a number concentration; whereas cloud ice is assumed to be monodispersed as a function of temperature. The rain, snow, and graupel/hail are assumed to be inverse exponential size distributions (Marshall and Palmer, 1948; Gunn and Marshall, 1958; Federer and Waldvogel, 1975). The precipitation in all types of water species is assumed to fall with mass-weighted mean terminal speed.

There are twelve prognostic variables containing velocity in x, y, z directions, pressure, potential temperature, turbulent kinetic energy, mixing ratio of water vapor, bulk cloud water, bulk cloud ice, bulk rain water, bulk snow aggregates, and bulk graupel/hail (Straka 1989). The Arakawa-C staggered grid (Arakawa and Lamb, 1981) is utilized in this model. The domain is 64 km × 64 km × 25 km with horizontal grid interval 500 m, and vertical interval 200 m. The time interval of integration is 2 seconds. The horizontal wind is subtracted, changing every 30 mins, to confine the convective activities within the computational domain. The upstream sixth-order, flux-conservative Crowley scheme is employed in advection terms (Tremback et al., 1987). Predictive variables are filtered every time step to handle nonlinear instability by a fourth-order numerical spatial diffusion operator (Klemp and Wilhelmson, 1978). A time filter is used in prognostic variables in the leapfrog scheme from odd and even time steps (Asselin, 1972). The radiation condition is utilized at the lateral boundaries to let patterns go out of domain without producing disturbances (Klemp and Wilhelmson, 1978). At the top boundary, all variables are given the values of the base state. A Rayleigh sponge layer is imposed to reduce gravity waves close to the top of the domain (Clark, 1977).

All the hydrometeor concentrations are shown as mixing ratios. Negative numbers of them do not set to null nor participate in any calculation. Such a design is to avoid false accumulation of water species, which happens when negative hydrometeors mixing ratios are set to zero. The convection is initiated by a thermal bubble, whose center is 2 km above ground level, with the maximum 3.5 K at bubble center and the radius 10 km and depth 4 km in the surrounding of horizontal homogeneousness. The relative humidity of the bubble is set to be the same as outside the thermal bubble by varying mixing ratio. A sensitivity study of the thermal bubble size was conducted and the results show that, while the numbers change somewhat, the main conclusions remain the same (see Sec. 5).

3. Simulation of the case Darwin

The three cases studied in this research with heavy rainfall over the Pacific Warm Pool are January 23, 2006, in Darwin, March 28, 2013, in Singapore, and July 18, 2013, in Medan. The Skew-T log-P soundings and wind fields of these storms are employed as the initial conditions in the numerical simulations (Figure 1). The properties of these soundings including the parameters and indices are summarized in Table 1. The significance of these parameters and indices will be discussed and compared with those in the storms in subtropics and High Plains in Section 5. The case of Darwin, 23 January 2006 is used as an example to show the verification with observation and to demonstrate simulated cloud microphysical features including the kinematics, thermodynamics, radar reflectivity, and precipitation over the Pacific Warm Pool.

After the initiation of a thermal anomaly, the maximum updraft exhibits two peaks with large vertical velocity due to the spin-up process associated with the initialization. Then the storm adjusts to a quasi-steady state in the mature stage from 150 min to 240 min. During this period, the maximum vertical velocity remains in the range of 12.7-28.8 m s^{-1} (Figure 2a). The simulated maximum updraft 25.9 m s^{-1} compares well to both the 90th percentile maximum vertical velocity of dual-Doppler-retrieved 3-D wind fields (Varble et al. 2014) and a root mean square (RMS) bias in the dual-Doppler retrieval (Collis et al. 2013) (Figure 2b). The algorithm for radar reflectivity is the same as that used in Stoelinga (2005). The radar reflectivity around the surface in the simulation is also close to the observation (Figure 2c). At higher altitudes, the reflectivity is larger than the observation as in some previous modeling results (Varble et al. 2014). Potential reasons such as size distribution assumption and slow hail mass-weighted fall speed were proposed to explain such larger upper radar reflectivity.

Figs. 3-4 show vertical cross-sections of the simulated hydrometeor mixing ratios, vertical velocity, and temperature. The mixing ratio of cloud water extends to at least 9 km altitude in the period from 150 min to 240 min. The corresponding temperature range is about 245-250 K. Cloud base is around 3 km during this period. The greatest cloud ice mixing ratio is located near, but not lower than, the levels of the largest vertical velocity. The cloud ice can be as low as 9 km (at about 230 K) or as high as 16 km (at about 190 K) (Figs. 3-4).

Typically rain occurs below 6 km. The maximum rain mixing ratios occur mostly close to local strong downdraft, either higher or lower than the levels of local maximum downdrafts, but rarely below the maximum updrafts. The maximum rain mixing ratio at surface is approximately 5.5 g kg^{-1}. The altitudes of snow (9-16 km) are closely linked with cloud ice and its mixing ratios are modulated by wind fields. The corresponding temperature range is 250-190 K. The wide spread of snow is due to several close convective cells and advection. Hail/graupel generally does not extend to as high as snow and cloud ice. At 180 min hail may reach a level as low as 2 km with strong downdraft. The maximum hail mixing ratio occurs at about 5-8 km height (Figs. 3-4).

During the quasi-steady mature stage, rain is distributed below 6 km, hail at about 3-13 km, and cloud ice and snow at about 9-16 km. Supercooled water is common during the mature stage whereas hail is usually above the altitudes of freezing point. The hail mixing ratio contours overlap the rain mixing ratio contours, and even extend to rain cores, and vice versa. This implies that the accretion of rain is a major source of hail, meanwhile, the melting of hail is an important source of rain (Figs. 3b-d, 4b-c).

4. Microphysical budget analysis of the case Darwin

We used the storm occurred at Darwin on 23 January 2006 as an example to demonstrate the details of Microphysical budget over the Pacific Warm Pool. The portion of liquid phase in total condensate mass gradually stabilizes after experiencing two minima and subsequently dominates after 148 min (Figs. 5a-b). The change of the percentage of liquid phase with time is 25%, 39%, 37%, 46%, 52%, 60%, 67%, and 61% of total condensate mass at 30, 60, 90, 120, 150, 180, 210, and 240 min, respectively, by careful examination of the data in Figure 5b. On average during quasi-steady stage over 150-240 min period with the data of every two mins, the portion of the liquid water phase in total condensate mass is about 62%. Individually, the percentages for cloud water, rain, cloud ice, snow, and hail in this period are about 25%, 37%, 3%, 18%, and 18% respectively. The mass of liquid water phase and ice phase over this period are about 2503 and 1559 KT. The individual mass of cloud water, rain, cloud ice, snow, and hail are about 988, 1515, 116, 725, and 718 KT, respectively (Figure 5). In contrast, the contribution of the liquid phase is on an average 20% and 46% in the High Plains and subtropics (Table 2 in LWS05), respectively. Hence, the liquid-phase dominate the thunderstorm hydrometeors in the case of Darwin.

The time evolution of the sources and sinks of rain, snow, and hail/graupel will be discussed below.

a. Rain

Figs. 6a and 7a show the rain sources and their respective percentage contributions. Melting from hail (qhmlr) is the leading rain source most of the time. It becomes increasingly important from the start and reaches a maximum at 60 min (Figs. 6a and 7a). At this time, abundant hail melts underneath the altitude of 273 K level with downdraft at lower levels (Figs. 3a and 4a). This follows the decrease of vertical velocity (Figure 2a) and peak hail generation at 50 min (Figure 5a). The melting of hail (qhmlr) then decreases (Figs. 6a and 7a) while hail production becomes smaller (Figure 5a) due to the dissipation of original storm (Figure 2a). The melting of hail (qhmlr) increases again (Figs. 6a and 7a) with greater hail generation (Figs. 2a and 5a) after that. Melting of hail (qhmlr) becomes the most significant process of rain production during 42-78 min and after 88 min (Figs. 6a and 7a). The accretion of cloud water (qracw) rises very quickly (Figs. 6a and 7a) as new storm develops (Figure 2a), and becomes a major rain source briefly (Figs. 6a and 7a). The evolution of shedding from hail (qhshr) (Figs. 6a and 7a) is similar to maximum updraft (Figure 2a).

In general, accretion (qracw), shedding of hail (qhshr), and melting of hail (qhmlr) are the major rain sources subsequent to 18 min. Melting of hail (qhmlr), which contributes mostly more than 40% of the total rain creation, remains the largest rain source. Shedding of hail(qhshr), which contributes mostly more than 30%, is the second one (Figs. 6a and 7a). Accretion of cloud water (qracw), which contributes about 20%, is the third one after 104 min except it exceeds shedding (qhshr) in 210-212 min. Figs. 6b and 7b show rain sinks and percentage contributions. For the most part, evaporation of rain (qrcev) and accretion of rain by hail (qhacr) are the two main rain sinks. Since most of the hydrometeors are liquid in the beginning, evaporation of rain (qrcev) is the most significant rain sink initially. Soon after the ice-phase processes develop much more quickly than evaporation (qrcev) and thus dominates until 68 min. After 80 min the rain depletion rate due to the accretion of rain by hail (qhacr) increases dramatically just when bountiful hail is generated (Figure 5a). Accretion of rain by hail (qhacr) is consequential in a large downdraft. After coming to its peak, the production rate of accretion of rain by hail (qhacr) (Figs. 6b and 7b) is essentially parallel to the hail evolution (Figure 5a).

Evaporation (qrcev) and accretion by hail (qhacr) remain the two major sinks, and accretion by ice, which contributes less than 12%, is the third one. Accretion by hail (qhacr) provides at least 31% rain depletion after 100 min. Accretion by snow (qsacr) contributes less than 3% rain depletion following 24 min, and thus can be neglected. After about 104 min evaporation (qrcev), accretion by hail (qhacr), and accretion by ice (qiacr) reach a quasi-steady state and average 50%, 42%, and 7% of the total sink rate, respectively (Figs. 6b, and 7b).

b. Snow

The dominant process of snow production is the Bergeron-Findeisen process, the transformation of cloud ice to snow (qsfi), which is larger than other processes almost all the time (Figs. 2a, and 6c). The Bergeron-Findeisen process (qsfi) occurs due to the difference of saturation vapor pressure over supercooled water and ice (see Wang, 2013) is more efficient than any other processes in snow production. The fact that the trend of maximum updraft is nearly parallel to the evolution of the Bergeron-Findeisen process (qsfi) suggests that the updraft moves cloud water upward to form supercooled water at middle and upper levels (Figs. 2a, and 6c).

The time evolution of snow production behaves as follows. Water vapor deposition to snow (qsdpv) occurs first. The transfer from cloud ice to snow in Bergeron-Findeisen process (qsfi) contributes no less than 41% of snow production subsequent to 16 min when it becomes the most significant snow source in simulation except at 12 min when vapor sublimation from snow (qssbv) surpasses it briefly. Accretion of cloud water (qsacw) continues to be the second largest source since 14 min. The production rate of deposition (qsdpv) becomes the third place after 34 min except for the contribution from the accretion of rain by ice (qiacr) overshadows deposition (qsdpv) briefly during 80-90 min. After 156 min the Bergeron-Findeisen process (qsfi), accretion of cloud water (qsacw), and deposition (qsdpv) approach a quasi-steady state, and average 47%, 34%, and 12% of total snow production rate, respectively (Figs. 6c, and 7c).

Accretion of snow by hail (qhacs) is the largest snow sink except for the first 10 min (Figure 6d). The peak of snow mass (at about 85 min) leading the peak of accretion by hail (qhacs) (at about 110 min) indicates the importance of snow depletion due to the accretion of snow aggregates by hail (qhacs) (Figs. 5a, and 6d). The time evolution of the sublimation of snow (qssbv) is similar to that of the accretion by hail (qhacs) except that the peak of sublimation (qssbv) occurs at about 115 min (Figure 6d).

Sublimation (qssbv) becomes and remains the second largest sink after 26 min. The depletion rate due to the melting of snow to rain (qsmlr) is similar to the accretion by rain (qhacs) but becomes larger after 144 minute. Accretion by hail (qracs), sublimation (qssbv), and melting (qsmlr) come to a quasi-steady state subsequent to 156 min, and average about 77%, 14%, and 7% of total snow sink rate, respectively (Figs. 6d, and 7d).

c. Hail/graupel

We will use hail to represent this category of hydrometeor in the following discussion. Accretion of rain by hail (qhacr), accretion of cloud water by hail (qhacw), and accretion of snow aggregates by hail (qhacs) are the top three production processes of hail after 40 min. Ample hail is produced in the initial spin-up period. Afterwards, the hail mass evolution is approximately parallel to the accretion of rain (qhacr). it is observed that the curve of accretion of rain (qhacr) lags hail mass progression. The hail production can be summarized as follows. After 108 min the accretion of rain (qhacr) becomes the leading mechanism except for the accretion of snow (qhacs) takes over briefly during 148-152 min. Accretion of rain (qhacr), cloud water (qhacw), and snow (qhacs) are the major processes and have similar production rates from 90 min on. These three processes become quasi-steady subsequent to 112 min, and average 37%, 30%, and 26% of total hail/graupel production rate, respectively (Figs. 6e, and 7e).

Rain shed from hail (qhshr) and melting of hail (qhmlr) to form rain are the two prime hail/graupel sinks all the time (Figs. 6f, and 7f). This is consistent with the previous observation that the shedding (qhshr) and melting (qhmlr) are mainly the utmost rain sources. Rain mass is the most plentiful of all hydrometeors during 62-80 min and after 114 min. Shedding (qhshr) and melting (qhmlr) reach the quasi-steady state after 112 min, and average 58%, and 41%, of total hail sink rate, respectively (Figs. 6f, and 7f).

A flow chart of the major microphysical processes is shown in Fig. 8. See the appendix for the microphysical meanings of the acronyms.

5. Comparison of microphysical budgets of storms over the Pacific Warm Pool with that in the subtropics and High Plains in LWS05

To comprehend the specialties in the microphysical processes over the Pacific Warm Pool, we will compare the microphysical budgets of precipitates over the Pacific Warm Pool with those in the subtropics and High Plains in LWS05 during the quasi-steady stage in this section.

The altitude for the melting of hails to start after they fall below the freezing level can be approximated by wet-bulb zero height. The wet-bulb zero height represents the minimum depth that a hail would fall without melting appreciably (Miller and McGinley 1977). The wet-bulb zero height over the Pacific Warm Pool is on the whole higher than in the subtropics and much higher than in the High Plains in LWS05. This shows that Pacific Warm Pool storms have lower potential to produce hail. Even existing hail would have melted in thick and warm low-level clouds before reaching the ground. The sub-cloud average mixing ratio of water vapor over the Pacific Warm Pool, in general, is more abundant in spite of lower surface temperatures than in the subtropics and much more abundant than in the High Plains in LWS05. The Warm Pool storms have lower and warmer cloud bases, implying that liquid-phase hydrometeors are more crucial. The lifting condensation levels (LCLs) and levels of free convection (LFCs) of the soundings over the Pacific Warm Pool are lower, but the equilibrium levels (ELs) are higher than in the subtropical and High Plains cases in LWS05. Therefore, the convective available potential energies (CAPEs) over the Pacific Warm Pool are larger than in the subtropics and High Plains in LWS05. In short, the characteristics of storm environment over the Pacific Warm Pool are close to those in the subtropics in LWS05, but they have more abundant moisture and are more prone to deep convection (see Table 1 and also Table 1 in LWS05).

On average the percentage of precipitation particles (rain, snow, and graupel/hail) in the total hydrometeor mass in storms over the Pacific Warm Pool (77.7%) is much less than in the subtropics (84.3%) and High Plains (84.6%) in LWS05. Even the largest percentage over the Pacific Warm Pool is less than the smallest one in the subtropics and High Plains in LWS05. In detail, the percentage of cloud water over the Pacific Warm Pool is much larger, but the percentage of hail is smaller than in the subtropics and High Plains in LWS05 due to higher temperature. Ice-phase hydrometeors (cloud ice, snow, and graupel/hail) over the Pacific Warm Pool (about 41%) are smaller than in the subtropics (about 54%) and High Plains (about 80%) in LWS05 (Table 2 and Table 2 in LWS05). In a nutshell, liquid-phase hydrometeors dominate in thunderstorms development over the Pacific Warm Pool.

To study how the hydrometeor partitioning would be sensitive to the bubble parameters over the Pacific Warm Pool, we conducted sensitivity tests to understand the effects of bubble width, height, position, and temperature perturbation. In the case of Singapore, the ratio of liquid-phase hydrometeors is about 61%. The thermal bubble is 2 km above ground level, with the maximum 3.5 K at bubble center and the radius 10 km and depth 4 km. When the thermal bubble is 4 km above ground, the ratio of liquid-phase hydrometeors is about 66%. The ratios for the maximum 2 K and 5 K cases are about 62% and 59%, respectively. The ratios for the depth 2 km and 6 km cases are about 56% and 60%, correspondingly. The ratios for the radius 5 and 20 km is 69% and 56%, respectively. In short, the sensitivity tests demonstrate that the dominance of liquid-phase hydrometeors in thunderstorm development over the Pacific Warm Pool is robust.

a. Rain

Melting of hail to rain (qhmlr) and accretion of cloud water by rain (qracw) are the two most significant rain sources over the Pacific Warm Pool (Table 3). The temperature over the Pacific Warm Pool is warmer and the updraft at lower levels is weaker than in the subtropics and High Plains in LWS05. Typically hail contours strongly overlap that of rain. The contours of 0.5 g kg^{-1} hail/graupel extend below the levels of 285 K and are close to the rain cores (Figs. 3-4). These indicate that melting of hail (qhmlr) is a very important source of rain, and more significant than shedding from hail (qhshr) when hail falls that is the difference in vertical cross-sections of hydrometeors between over the Pacific Warm Pool and in the subtropics (Figs. 4-5 in LWS05). Hence, melting of hail (qhmlr) over the Pacific Warm Pool (about 40%) on average contributes more than in the subtropics (about 30%); whereas the contribution of shedding from hail (qhshr) over the Pacific Warm Pool (about 31%) is between in the subtropics (about 45%) and High Plains (about 20%) in LWS05 (Figs. 8a-b, and Figs. 16a-b in LWS05). Although melting is more important than shedding in the High Plains, the conditions of hail separating from rain, no strong wet growth, and few raindrops being collected (LWS05) are very different from the Pacific Warm Pool. Because of high temperature and large humidity in tropical Pacific Warm Pool, cloud water tends to develop instead of freezing, and thus, has more chance to undergo collision and coalescence to form rain. Therefore, accretion of cloud water by rain (qracw) over the Pacific Warm Pool (about 26%) contributes more than in the subtropics (about 20%) and High Plains (about 5%) (Figure 9c and Figure 16c in LWS05).

Accretion of rain by hail (qhacr) and evaporation of rain (qrcev) are the two dominant rain sinks over the Pacific Warm Pool (Table 3). These two processes contribute more than 88% of rain depletion in all three cases. Generally, rain stays at low levels. The humidity at lower level determines the dominant sinks (Figure 1 and Table 3). Because of larger updraft and more significant overlap of hail and rain regions in the subtropical case CaPE (0729) in LWS05 (Figs. 3-5 in LWS05), accretion by hail (qhacr) is more important in rain depletion in the subtropics (about 65%) than over the Pacific Warm Pool (about 50%). In addition to accretion by hail (qhacr), the updraft in a quasi-steady state of CaPE (0729) in LWS05 (Figure 3 in LWS05) is larger than over the Pacific Warm Pool (Figure 2a). Therefore, more rain is brought aloft in the subtropics in LWS05 that leads to the larger accretion of supercooled water by ice and snow (qiacr, and qsacr) than over the Pacific Warm Pool. The accretions of supercooled water by ice and snow (qiacr, and qsacr) in the subtropics in LWS05 account for more rain depletion than over the Pacific Warm Pool (Figs. 9c-d and Figs. 17c-d in LWS05). Conversely, the contribution of evaporation (qrcev) in the subtropics in LWS05 (about 20%) is less than over the Pacific Warm Pool (about 40%) on average (Figure 10b and Figure 17b in LWS05).

b. Snow

The ranking of snow sources over the Pacific Warm Pool is similar to the subtropics (Table 4 and Table 4 in LWS05). Bergeron-Findeisen process of cloud ice to snow (qsfi) is the chief process and is on average more efficient in the subtropics in LWS05 (about 70%) than over the Pacific Warm Pool (about 57%) (Figure 11a, and Figure 18a in LWS05). Due to larger snow concentration and lower cloud base over the Pacific Warm Pool (Figs. 3-4 and Figs. 4-5 in LWS05) accretion of cloud water (qsacw) is more dominant over the Pacific Warm Pool (about 25%) than in the subtropics in LWS05 (about 15%) (Figure 11b, and Figure 18b in LWS05). Both Bergeron-Findeisen process of cloud ice to snow (qsfi) and accretion of cloud water (qsacw) generally account for about 83% of snow production during the quasi-steady stage over the Pacific Warm Pool. Becuase of higher levels of snow over the Pacific Warm Pool (Figs. 3-4 and Figs. 4-5 in LWS05) less water vapor accompanied by larger snow concentration gives rise to more essential vapor deposition to snow (qsdpv) (about 9%) than in the subtropics in LWS05 (about 4%). Accretion of cloud ice (qsaci) and accretion of rain by ice (qiacr) play about equal role over the Pacific Warm Pool and in the subtropics in LWS05 (Figure 11c, and Figs. 11c, and 18c in LWS05).

The ranking of snow sinks over the Pacific Warm Pool is close to that in the subtropics and High Plains in LWS05 (Table 4 and Table 4 in LWS05). The contribution of about 80% of snow depletion due to accretion by hail (qhacs) over the Pacific Warm Pool is similar to that in the subtropics and High Plains in LWS05 as well (Figure 12a, and Figure 19a in LWS05). Vapor sublimation of snow (qssbv) accounts for 15% of snow depletion over the Pacific Warm Pool, roughly the same as those in the subtropics and High Plains in LWS05 (Figure 12b, and Figure 19b in LWS05). The significance of accretion of snow by rain to form snow or hail (qracs) over the Pacific Warm Pool (about 3%) is also similar to those in the subtropics in LWS05 (Figure 12c, and Figure 19c in LWS05).

c. Hail/graupel

The order of ranking of hail sources over the Pacific Warm Pool is similar to the subtropics in LWS05 (Table 5 and Table 5 in LWS05), but the percentage contributions of the major three hail sources, accretion of rain (qhacr), accretion of cloud water (qhacw), and accretion of snow (qhacs), over the Pacific Warm Pool are a bit different from in the subtropics in LWS05. Larger updraft in the subtropics (Figure 2a, and Figure 3 in LWS05) enables more accretion of supercooled water (about 50%) than over the Pacific Warm Pool (about 40%) (Figure 13a, and Figure 20a in LWS05). The accretion of rain by hail (qhacr) is more efficient than the accretion of cloud water by hail (qhacw) (about 30%) (Figure 13b, and Figure 20b in LWS05). Larger snow concentration over the Pacific Warm Pool results in more accretion of snow (qhacs) (about 22%) than in the subtropics in LWS05 (about 10%) (Figure 13c, and Figure 20c in LWS05). Due to larger updraft the accretions of supercooled by ice (qiacr) and snow (qsacr) to form snow or hail in the subtropics in LWS05 (about 7% and 3%, respectively) are larger than over the Pacific Warm Pool (about 5% and 1%, respectively) (Figs. 12d-e, and Figs. 20d-e in LWS05).

The ranking of hail sinks over the Pacific Warm Pool is the same as the High Plains in LWS05 (Table 5 and Table 5 in LWS05). Both melting of hail (qhmlr) and shedding from hail (qhshr) contribute about 99% of hail depletion over the Pacific Warm Pool (Figure 14). Melting of hail (qhmlr) (about 55%) is more important than shedding from hail (qhshr) (about 44%) over the Pacific Warm Pool that is very different from the subtropics where shedding from hail (qhshr) (about 60%) is more important than melting of hail (qhmlr) (about 40%) (Figs. 13a-b, and Figs. 21a-b in LWS05). In the High Plains in the LWS05 melting of hail (qhmlr) (about 75%) is much more efficient than shedding from hail (qhshr) (about 20%). The microphysical conditions in High Plains that hail region separates from rain, no strong wet growth happens, and little rain is collected as hail falls (LWS05) are completely different from the Pacific Warm Pool. Due to higher temperature and moisture, water vapor sublimation from hail (qhsbv) over the Pacific Warm Pool (0.8%) is less efficient than in the subtropics (1%) and High Plains (3%) in LWS05.

6. Summary

In this study, we have employed a microphysical model WISCDYMM to investigate the dynamics, thermodynamics, the details of hydrometeors, and the development microphysical budgets during quasi-steady stage over the Pacific Warm Pool. In addition, we have examined the differences in hydrometeor partitioning and cloud microphysical processes between the Pacific Warm Pool, the subtropics, and High Plains in LWS05.

During the mature stage, supercooled water is common. The hail mixing ratio contours overlap significantly with that of rain. Furthermore, the hail mixing ratio contours get as far as rain cores and the rain mixing ratio contours extend to hail cores, which shows that the melting of hail is an important source of rain and that the accretion of rain is a major source of hail.

Microphysical budgets depend on atmospheric dynamical and thermodynamical conditions and give the partitioning information of hydrometeors. Liquid-phase hydrometeors govern thunderstorm development over the Pacific Warm Pool. The ratio of ice-phase mass to liquid-phase mass is about 41% : 59% (Table 2) over the Pacific Warm Pool, compared with 54% : 46% in the subtropics and 80% : 20% in the High Plains (Table 2 in LWS05). The sensitivity tests on bubble width, height, position, and temperature perturbation indicate that the domination of liquid-phase hydrometeors in thunderstorm development over the Pacific Warm Pool is potent.

The principal microphysical processes over the Pacific Warm Pool are as follows. The main rain sources are also the key hail sinks, namely, melting of hail and shedding from hail; whereas the crucial rain sinks are accretion by hail and evaporation. The major snow sources are Bergeron-Findeisen process, transfer of cloud ice to snow, and accretion of cloud water; whereas the foremost snow sink is accretion by hail. The essential hail sources are accretions of rain, cloud water, and snow; whereas the most important hail sinks are melting of hail and shedding from hail. The contribution and ranking of sources and sinks of these precipitates have been compared with those in the subtropics and High Plains in LWS05.

Microphysical budgets are closely associated with cloud radiative properties. Cloud-radiation interactions would lead to the changes in climate. Therefore, a clear understanding of such microphysical processes is not only important in estimating the performance of cloud models and products of passive satellite measurements but also helps to develop a proper parameterization of moist processes in climate models.

The sounding data decide atmospheric dynamical and thermodynamical conditions, and thus the hydrometeor partitioning and cloud microphysical processes. Microphysical processes are highly nonlinear in themselves. A comprehensive and thorough study is necessary to understand clear connections between them. This knowledge will ultimately benefit the microphysics parameterization and cumulus parameterization in global circulation and climate models.

Acknowledgments

This study is partially supported by NOAA GOES-R contract 9636, Risk Reduction Award NA10NES4400013, National Science Foundation Grant AGS-1219586 and AGS- 1633921, and research fund support from Academia Sinica and Ministry of Science and Technology, Taiwan. Any opinions, findings and conclusions or recommendations expressed in this material are those of the authors and do not necessarily reflect the views of the National Science Foundation (NSF). The authors also thank the helpful comments of two anonymous reviewers that led to improvements of the paper.

References

Anderson, J.R., Droegemeier, K.K., Wilhelmson, R.B., 1985. Simulation of the thunderstorm subcloud environment, paper presented at Conference on Severe Local Storms. Am. Meteorol. Soc., Indianapolis, Indiana.

Arakawa, A., Lamb, V.R., 1981. A potential enstrophy conserving scheme for the shallow water equations. Mon. Wea. Rev. 109, 18 – 36.

Asselin, R., 1972. Frequency filter for time integrations. Mon. Wea. Rev. 100, 487 – 490.

Barlow, M., Cullen, H., Lyon, B., 2002. Drought in central and southwest Asia, La Niña, the Pacific Warm Pool and Indian Ocean precipitation. J. Clim. 15, 697 – 700.

Chen, B., Yin, Y., 2011. Modeling the impact of aerosols on tropical overshooting thunderstorms and stratospheric water vapor. J. Geophys. Res. 116, D19203, doi:10.1029/2011JD015591.

Clark, T.L., 1977. A small scale dynamic model using a terrain-following coordinate transformation. J. Comput. Phys. 24, 186 – 215.

Collis, S., Protat A., May, P.T., Williams, C., 2013. Statistics of storm updraft velocities from TWP-ICE including verification with profiling measurements. J. Appl. Meteorol. Climatol. 52, 1909 – 1922.

Cotton, W.R., Stephens M.A., Nehrkorn, T., Tripoli, G.J., 1982. The Colorado State University three-dimensional cloud model – 1982, part II, An ice phase parameterization. J. Rech. Atmos. 16, 295 – 320.

Cotton, W.R., Tripoli, G.J., Rauber, R.M., Mulvihill, E.A., 1986. Numerical simulation of the effects of varying ice crystal nucleation rates and aggregation processes on orographic snowfall. J. Clim. Appl. Meteorol. 25, 1658 – 1680.

Federer, B., Waldvogel, A., 1975. Hail and raindrop size distributions from a Swiss multicell storm. J. Appl. Meteorol. 14, 91 – 97.

Hourdin, F., Musat, I., Bony, S., Braconnot, P., Codron, F., Dufresne, J.L., Fairhead, L., Filiberti, M.A., Friedlingstein, P., Grandpeix, J.Y., Krinner, G., Levan, P., Li, Z.X., Lott, F., 2006. The LMDZ4 general circulation model: climate performance and sensitivity to parametrized physics with emphasis on tropical convection. Clim. Dynam. 27, 787 - 813.

Gunn, K.L.S., Marshall, J.S., 1958. The distribution with size of snow aggregates. J. Meteorol. 15, 452 – 461.

Johnson, D.E., Wang, P.K., Straka, J.M., 1993. Numerical simulation of the 2 August 1981 CCOPE supercell storm with and without ice microphysics. J. Appl. Meteorol. 32, 745 – 759.

Johnson, D.E., Wang, P.K., Straka, J.M., 1994. A study of microphysical processes in the 2 August 1981 CCOPE supercell storm. Atmos. Res. 33, 93 – 123.

Klemp, J.B., Wilhelmson, R.B., 1978. The simulation of three-dimensional convective storm dynamics. J. Atmos. Sci. 35, 1070 – 1096.

Li, X., Shen, X., 2013. Rain microphysical budget in the tropical deep convective regime: a 2-D cloud-resolving modeling study. J. Meteor. Soc. Japan. 91(6), 801 - 815.

Li, X., Shen, X., Liu, J., 2011. A partitioning analysis of tropical rainfall based on cloud budget. Atmos. Res. 102, 444 - 451.

Lin, H.-M., Wang, P.K., Schlesinger, R.E., 2005. Three-dimensional nonhydrostatic simulations of summer thunderstorms in the humid subtropics versus High Plains. Atmos. Res., 78, 103 - 145.

Lin, Y.-L., Farley R.D., Orville, H.D., 1983. Bulk parameterization of the snow field in a cloud model. J. Clim. Appl. Meteorol. 22, 1065 – 1092.

Marshall, J.S., Palmer, M., 1948. The distribution of raindrops with size. J. Meteorol. 5, 165 – 166.

Miller, R.C., McGinley, J.A., 1977. Response to "Inherent Difficulties in Hail Probability Prediction" and "Forecasting Hailfall in Alberta". Mefeorol. Monogr. 38, 153 - 154.

Randall, D.A., Wood, R.A., Bony, S., Colman, R., Fichefet, T., Fyfe, J., Kattsov, V., Pitman, A., Shukla, J., Srinivasan, J., Stouffer, R.J., Sumi, A., Taylor, K.E., 2007. Climate Models and Their Evaluation. In: Climate Change 2007: The Physical Science Basis. Contribution of Working Group I to the Fourth Assessment Report of the Intergovernmental Panel on Climate Change. [Solomon, S., D. Qin, M. Manning, Z. Chen, M. Marquis, K.B. Averyt, M.Tignor and H.L. Miller (eds.)]. Cambridge University Press, Cambridge, United Kingdom and New York, NY, U.S.A.

Straka, J.M., 1989. Hail growth in a highly glaciated central high plains multicellular hailstorm. Ph.D. thesis, Univ. of Wisc.-Madison, U.S.A., 413 pp.

Stoelinga, M.T., 2005. Simulated equivalent reflectivity factor as currently formulated in RIP: Description and possible improvements. www.atmos.washington.edu/~stoeling/**RIP**_sim_ref.pdf.

Takahashi, T., Keenan, T.D., 2004. Hydrometeor mass, number, and space charge distribution in a ''Hector'' squall line. J. Geophys. Res. 109, D16208, doi:10.1029/2004JD004667.

Tremback, C., Powell, J., Cotton, W.R., Pielke, R.A., 1987. The forward-in-time upstream advection scheme: Extension to higher orders. Mon. Wea. Rev. 115, 540 – 555.

Varble, A., Zipser, E.J., Fridlind, A.M., Zhu, P., Ackerman, A.S., Chaboureau, J.-P., Collis, S., Fan, J., Hill, A., Shipway, B., 2014. Evaluation of cloud-resolving and limited area model intercomparison simulations using TWP-ICE observations: 1. Deep convective updraft properties. J. Geophys. Res. Atmos. 119, 13,891 – 13,918.

Wang, P.K., 2003. Moisture plumes above thunderstorm anvils and their contributions to cross tropopause transport of water vapor in midlatitudes. J. Geophys. Res. 108 (D6), 4194.

Wang, P.K., 2003. Physics and Dynamics of Clouds and Precipitation. Cambridge University Press, 467pp.

Wang, B., Xie, X., 1998. Coupled Modes of the Pacific Warm Pool Climate System Part I: The Role of Air-Sea Interaction in Maintaining Madden-Julian Oscillation. J. Climate, 11, 2116 - 2135.

Table Captions

Table 1. Characteristics and indices of the observed soundings over the Pacific Warm Pool

Table 2. Time-averaged partitioning of the domain-integrated hydrometeor masses during the quasi-steady stage of each simulated storm

Table 3. Rankings of the domain-integrated individual sources and sinks of rain

Table 4. As in Table 3, but for snow

Table 5. As in Table 3, but for hail

Table 1

Characteristics and indices of the observed soundings over the Pacific Warm Pool

		Pacific Warm Pool		
		Darwin 1/23/2006	Singapore 3/ 28/2013	Medan 7/18/2013
Sub-cloud average mixing ratio (g/kg)		20	18	17
Surface	P (m b)	998	995	996
	T (° C)	28.1	27.5	27.4
LCL	P (m b)	970.34	964.23	937.29
	T (° C)	25.66	24.07	21.88
LFC	P (m b)	888.70	922.53	833.51
	T (° C)	22.55	22.44	17.49
EL	P (m b)	100.73	102.81	119.45
	T (° C)	-82.35	-84.82	-79.80
CAPE (J/kg)		3941	3725	3667
CIN (J/kg)		6	2	13
Total totals index		47	46	48
Lift index		-5	-5	-7
Showalter index		-2.9	-3.5	-2.1
K index		40	41	41
Deep convective index		44.5	42.7	39.1
Severe weather threat index		343	257	246
Wet bulb zero m (AGL)		5130	4824	4149

Table 2

Time-averaged partitioning of the domain-integrated hydrometeor masses during the quasi-steady stage of each simulated storm

	Pacific Warm Pool (%)		
	Darwin	Singapore	Medan
Cloud water	25	16	15
Rain	37	45	39
Cloud ice	3	4	4
Snow	18	15	21
Hail	17	20	21
Precipitates	72	80	81
Non- precipitates	28	20	19
Snow + Hail	35	35	42
Ice phases	38	39	46
Liquid phases	62	61	54

Table 3
Rankings of the domain-integrated individual sources and sinks of rain

		Pacific Warm Pool		
		Darwin	Singapore	Medan
Production	qhshr	2	3	2
	qhmlr	1	2	1
	qracw	3	1	3
	qrcnw	4	4	4
	qsmlr	5	5	5
	qsacw	6	6	6
Depletion	qhacr	2	1	1
	qrcev	1	2	2
	qiacr	3	3	3
	qsacr	4	4	4
	qrfrz	5	5	5

Table 4
As in Table 3, but for snow

		Pacific Warm Pool		
		Darwin	Singapore	Medan
Production	qsfi	1	1	1
	qsacw	2	2	2
	qsdpv	3	4	3
	qsaci	5	5	5
	qiacr	4	3	4
	qsacr	6	6	6
	qscni	7	7	7
	qraci	9	9	9
	qrfrz	8	8	8
	qsfw	10	10	10
Depletion	qhacs	1	1	1
	qssbv	2	2	2
	qracs	4	3	3
	qsmlr	3	4	4
	qhcns	5	5	5

Table 5
As in Table 3, but for hail

		Pacific Warm Pool		
		Darwin	Singapore	Medan
Production	qhacr	1	1	1
	qhacw	2	2	2
	qhacs	3	3	3
	qiacr	4	4	4
	qsacr	5	5	5
	qhdpv	6	6	6
	qhaci	8	7	7
	qracs	7	8	8
	qhcns	9	9	9
	qrfrz	10	10	10
	qraci	11	11	11
Depletion	qhshr	2	2	2
	qhmlr	1	1	1
	qhsbv	3	3	3

Figure Captions

Figure 1. Skew T – log P diagram at (a) Darwin, Northern Territory, Australia at 1200 UTC on 23 January 2006; (b) Singapore at 0000 UTC on 28 March 2013; (c) Medan, Indonesia at 1200 UTC on 18 July 2013.

Figure 2. (a) Time evolution of the maximum vertical velocity (m s^{-1}), (b) the 50th percentile (blue), and 90th percentile (red) of maximum vertical velocity (m s^{-1}), and (c) the 50th percentile (blue), 90th percentile (red), and 99th percentile (green) maximum radar reflectivity (dBZ) in the simulation for the case of Darwin, 23 January 2006.

Figure 3. Simulated hydrometeor mixing ratios, vertical velocity (shaded), and temperature (gray) for the case of Darwin on 23 January 2006 in X-Z vertical cross-sections through the maximum updraft as of (a) 150 min, (b) 180 min, (c) 210 min, and (d) 240 min. The minimum values of cloud water (green), rain (pink), cloud ice (cyan), snow (blue) and graupel/hail (black) are 1, 0.5, 0.5, 0.5, and 0.5 g kg^{-1}, respectively. The intervals of these hydrometeors are 0.5, 0.5, 0.2, 0.2, and 0.5 g kg^{-1}, respectively.

Figure 4. As in Figure 3 but in Y-Z vertical cross-sections.

Figure 5. Time evolution of simulated (a) total condensate mass and (b) percentage contribution, integrated over the entire simulation domain (64×64×18.4 km^3), for cloud water (blue), rain (red), cloud ice (green), snow (purple), and hail/graupel (cyan) in the case of Darwin, 23 January 2006.

Figure 6. Sources and sinks of each precipitating hydrometeor class for the Darwin, 23 January 2006 storm: (a) rain sources, (b) rain sinks, (c) snow sources, (d) snow sinks, (e) hail/graupel sources, (f) hail/graupel sinks. See the appendix for the microphysical meanings of the acronyms.

Figure 7. As in Figure 6 but that the precipitating hydrometeor sources and sinks are plotted by percentage contributions.

Figure 8. A flow chart of all microphysical processes. Red capital letters are the major ones. See the appendix for the microphysical meanings of the acronyms.

Figure 9. Superimposed time series in all three storm simulations for the rain sources: (a) qhshr, (b) qhmlr, (c) qracw. See the appendix for the microphysical meanings of the acronyms.

Figure 10. Superimposed time series in all three storm simulations for the rain sinks: (a) qhacr, (b) qrcev, (c) qiacr, (d) qsacr, (e) qrfrz. See the appendix for the microphysical meanings of the acronyms.

Figure 11. Superimposed time series in all three storm simulations for the snow sources: (a) qsfi, (b) qsacw, (c) qsdpv, (d) qsaci, (e) qiacr. See the appendix for the microphysical meanings of the acronyms.

Figure 12. Superimposed time series in all three storm simulations for the snow sinks : (a) qhacs, (b) qssbv, (c) qracs. See the appendix for the microphysical meanings of the acronyms.

Figure 13. Superimposed time series in all three storm simulations for the hail/graupel sources: (a) qhacr, (b) qhacw, (c) qhacs, (d) qiacr, (e) qsacr. See the appendix for the microphysical meanings of the acronyms.

Figure 14. Superimposed time series in all three storm simulations for the hail/graupel sinks: (a) qhshr, (b) qhmlr, (c) qhsbv. See the appendix for the microphysical meanings of the acronyms.

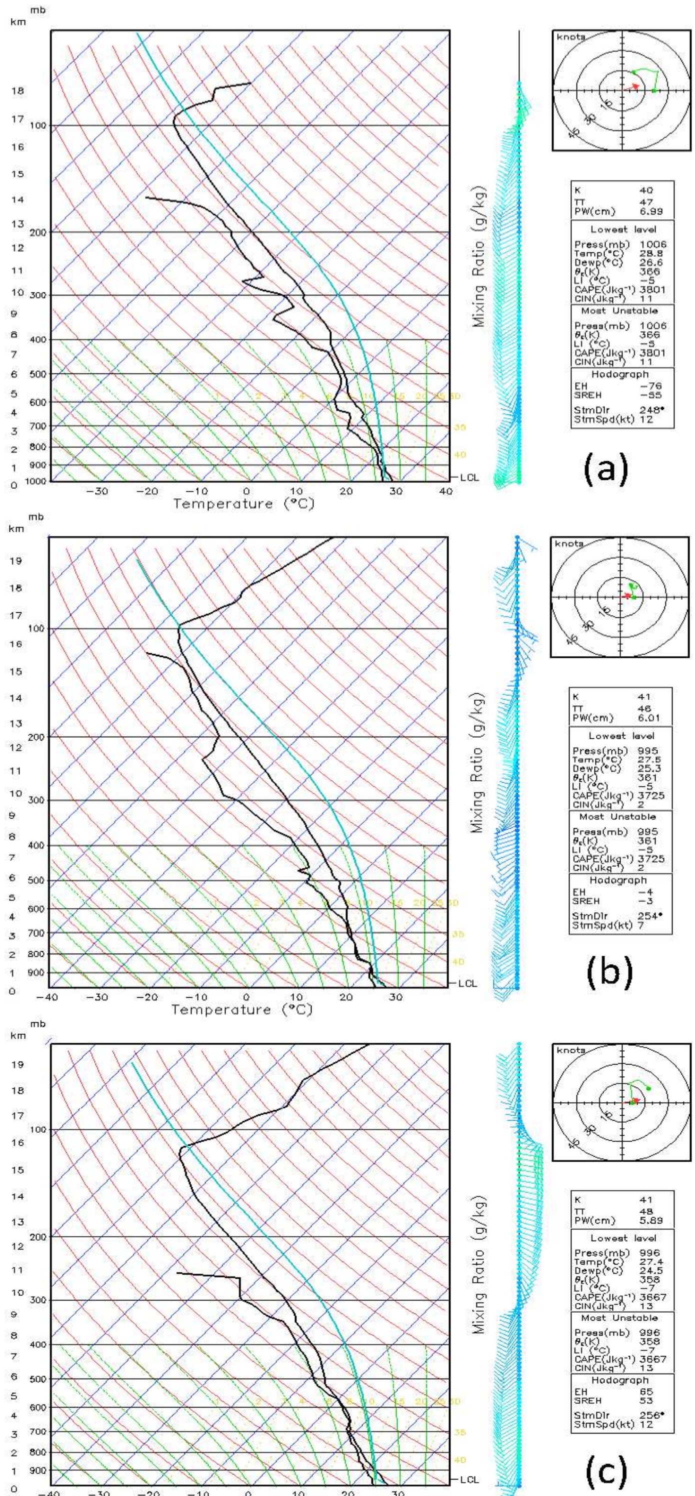

Figure 1. Skew T – log P diagram at (a) Darwin, Northern Territory, Australia at 1200 UTC on 23 January 2006; (b) Singapore at 0000 UTC on 28 March 2013; (c) Medan, Indonesia at 1200 UTC on 18 July 2013.

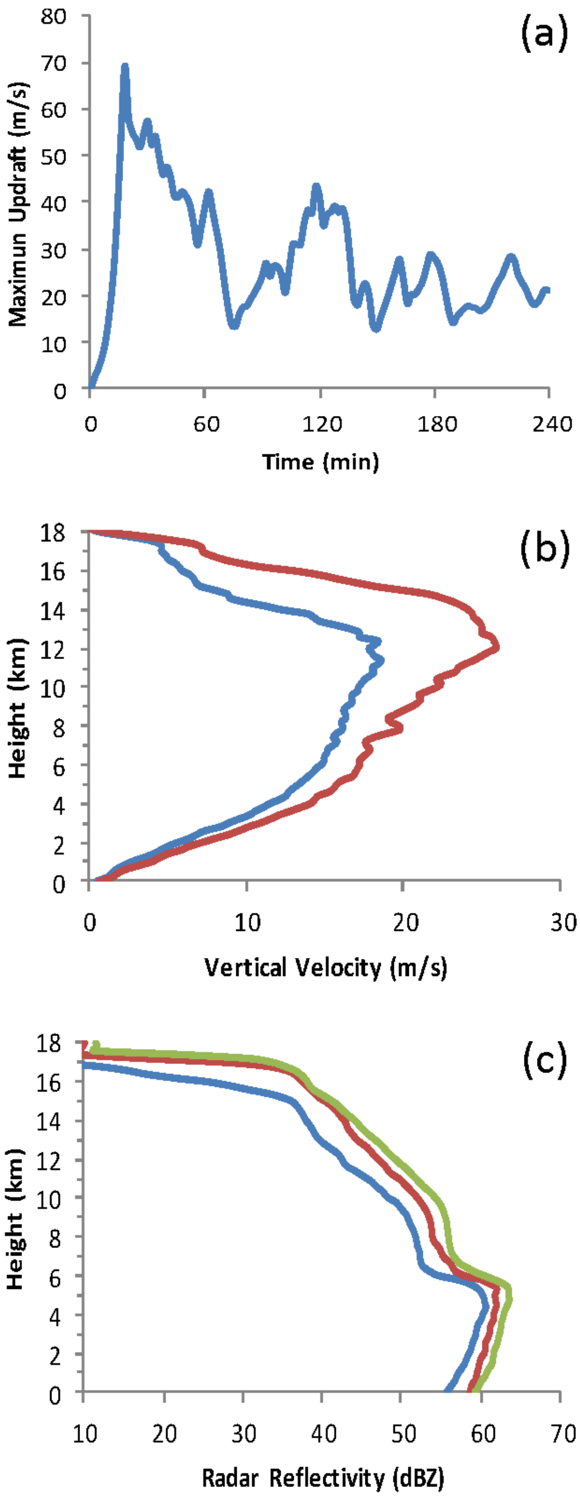

Figure 2. (a) Time evolution of the maximum vertical velocity (m s^{-1}), (b) the 50th percentile (blue), and 90th percentile (red) of maximum vertical velocity (m s^{-1}), and (c) the 50th percentile (blue), 90th percentile (red), and 99th percentile (green) maximum radar reflectivity (dBZ) in the simulation for the case of Darwin, 23 January 2006.

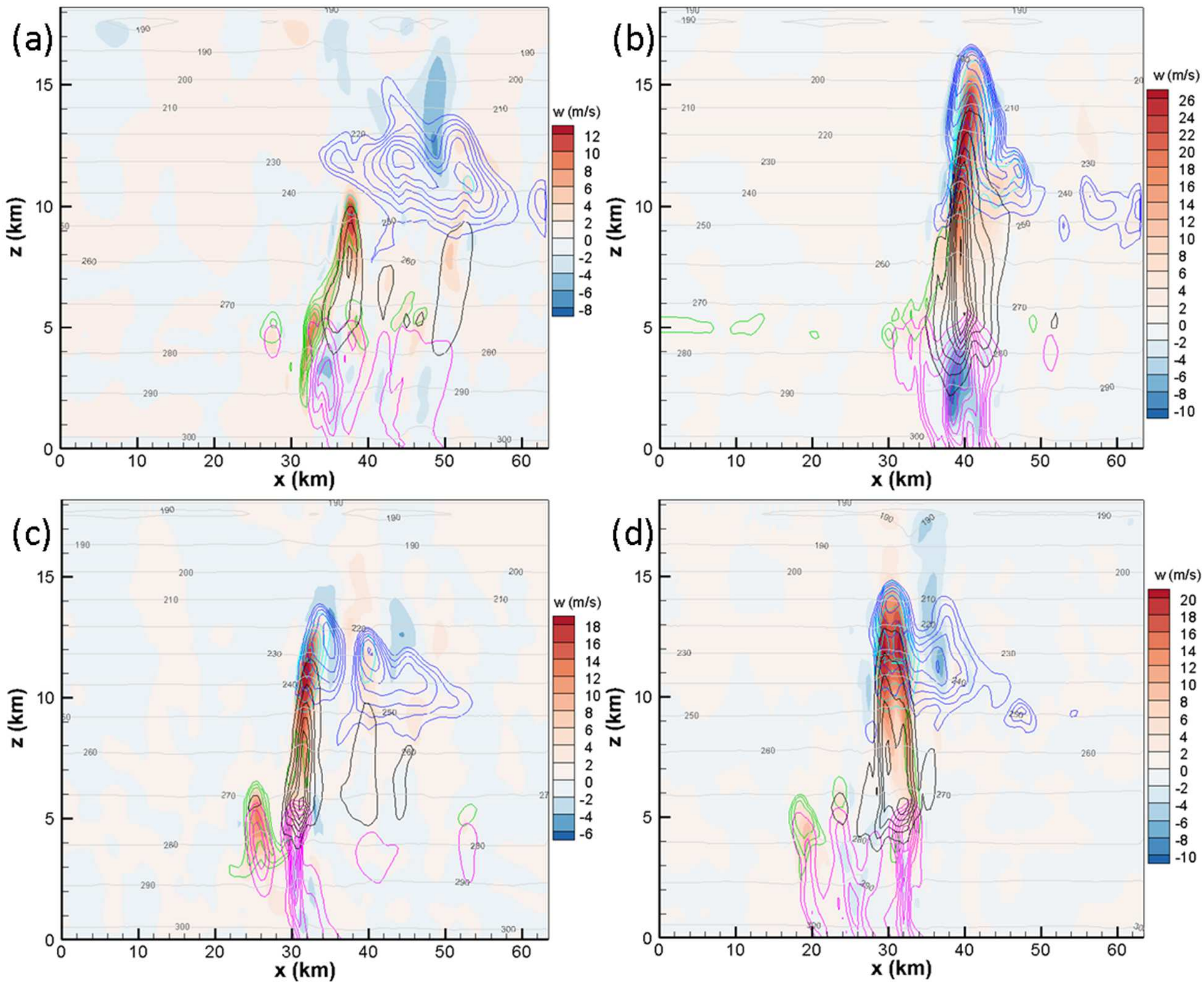

Figure 3. Simulated hydrometeor mixing ratios, vertical velocity (shaded), and temperature (gray) for the case of Darwin on 23 January 2006 in X-Z vertical cross-sections through the maximum updraft as of (a) 150 min, (b) 180 min, (c) 210 min, and (d) 240 min. The minimum values of cloud water (green), rain (pink), cloud ice (cyan), snow (blue) and graupel/hail (black) are 1, 0.5, 0.5, 0.5, and 0.5 g kg^{-1}, respectively. The intervals of these hydrometeors are 0.5, 0.5, 0.2, 0.2, and 0.5 g kg^{-1}, respectively.

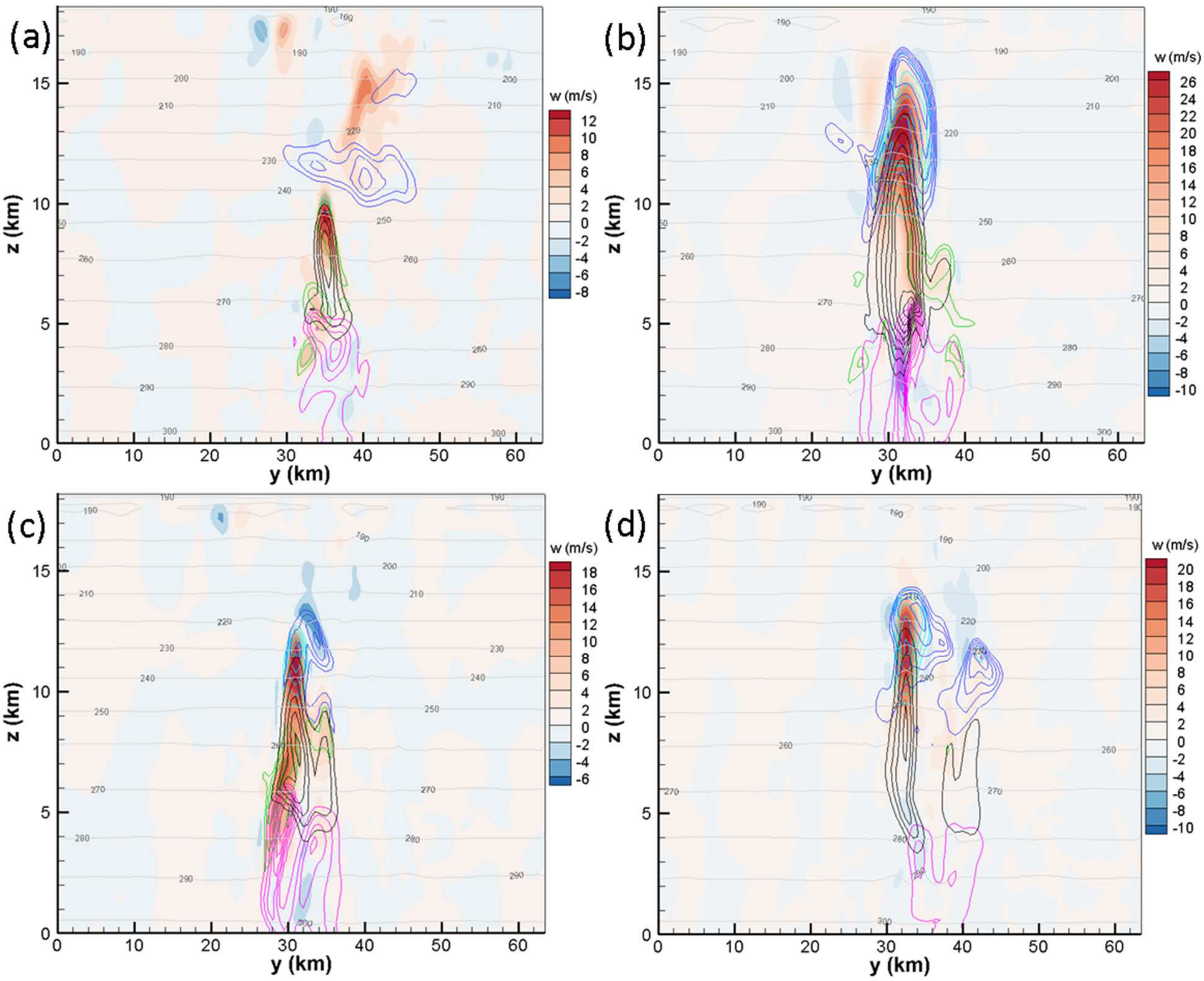

Figure 4. As in Figure 3 but in Y-Z vertical cross-sections.

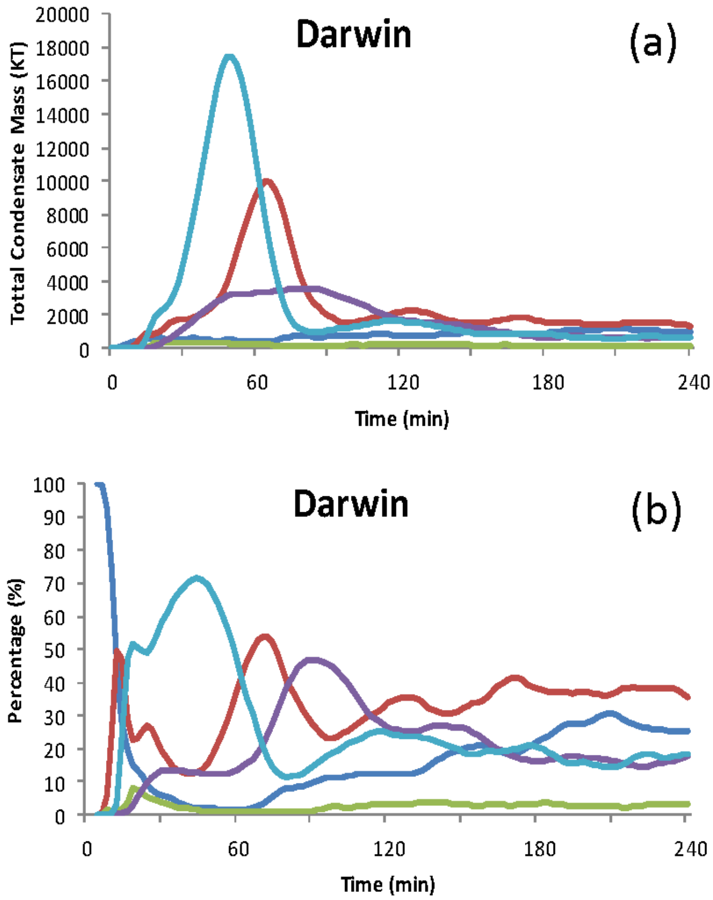

Figure 5. Time evolution of simulated (a) total condensate mass and (b) percentage contribution, integrated over the entire simulation domain (64×64×18.4 km^3), for cloud water (blue), rain (red), cloud ice (green), snow (purple), and hail/graupel (cyan) in the case of Darwin, 23 January 2006.

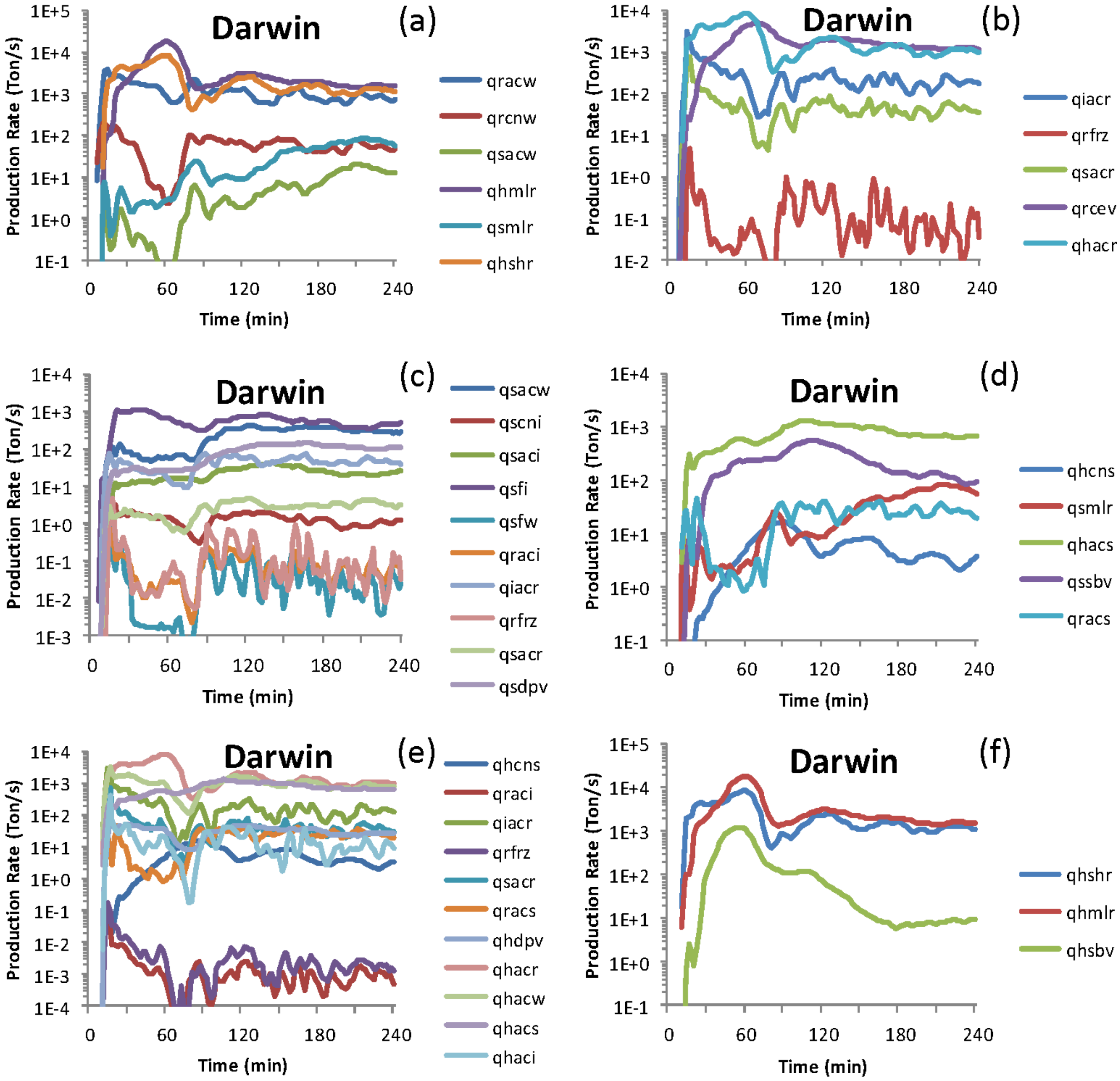

Figure 6. Sources and sinks of each precipitating hydrometeor class for the Darwin, 23 January 2006 storm: (a) rain sources, (b) rain sinks, (c) snow sources, (d) snow sinks, (e) hail/graupel sources, (f) hail/graupel sinks. See the appendix for the microphysical meanings of the acronyms.

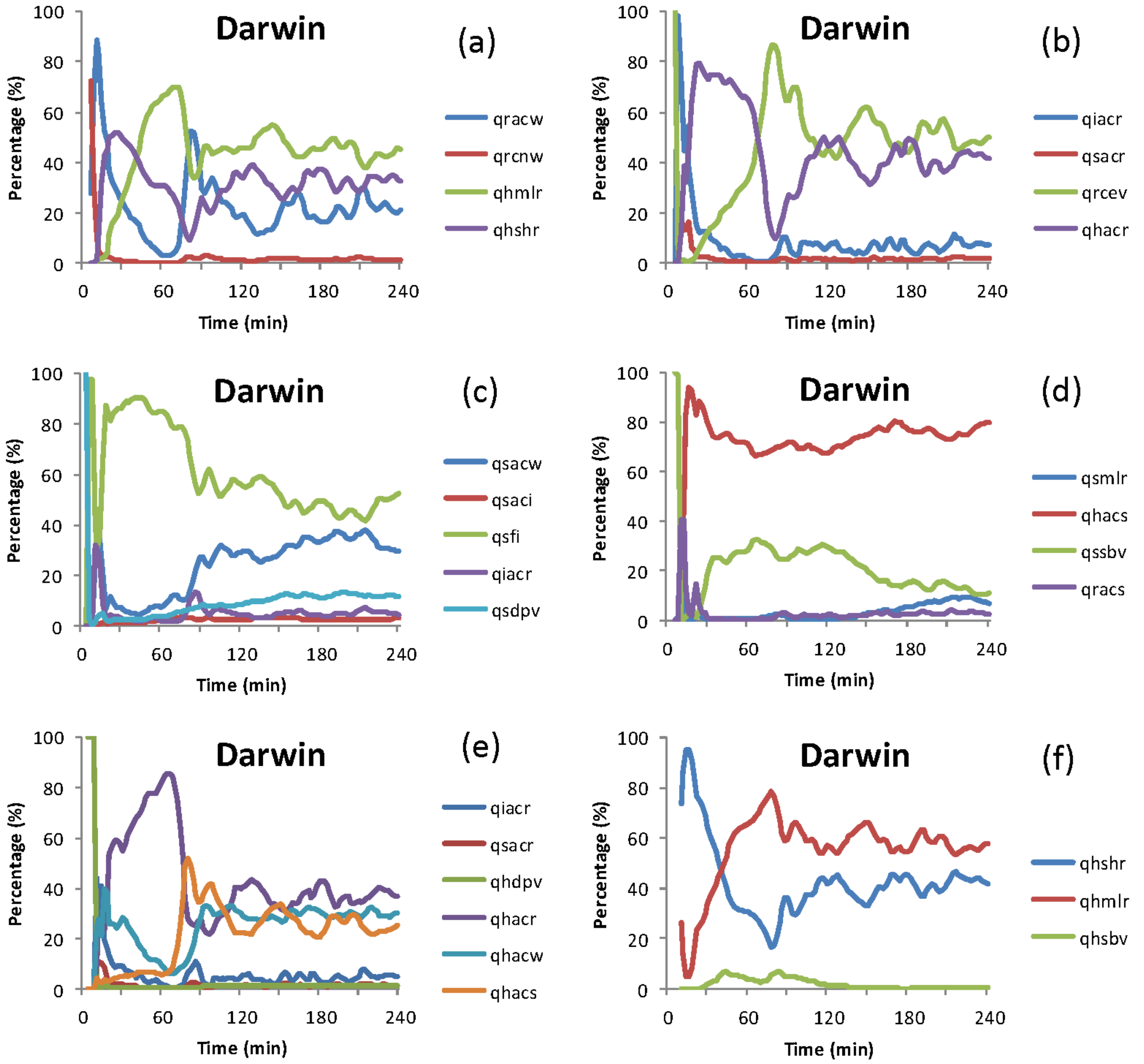

Figure 7. As in Figure 6 but that the precipitating hydrometeor sources and sinks are plotted by percentage contributions.

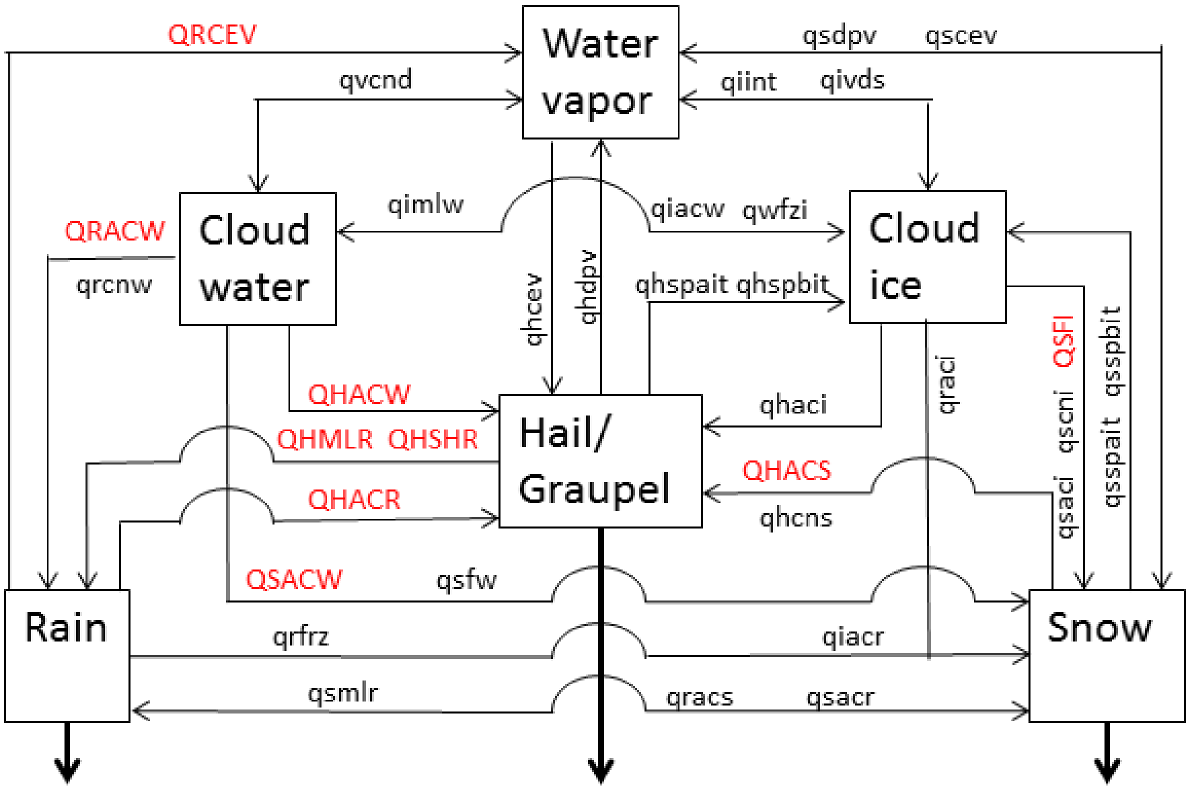

Figure 8. A flow chart of all microphysical processes. Red capital letters are the major ones. See the appendix for the microphysical meanings of the acronyms.

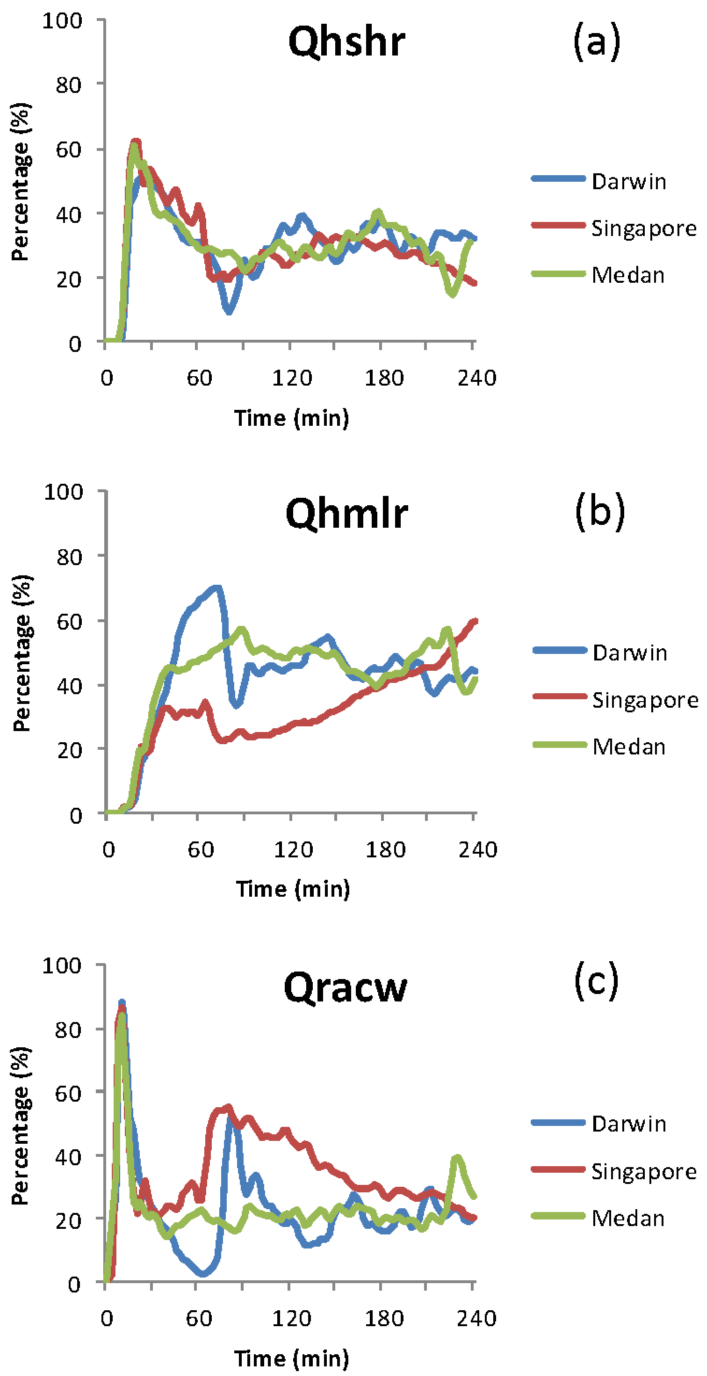

Figure 9. Superimposed time series in all three storm simulations for the rain sources: (a) qhshr, (b) qhmlr, (c) qracw. See the appendix for the microphysical meanings of the acronyms.

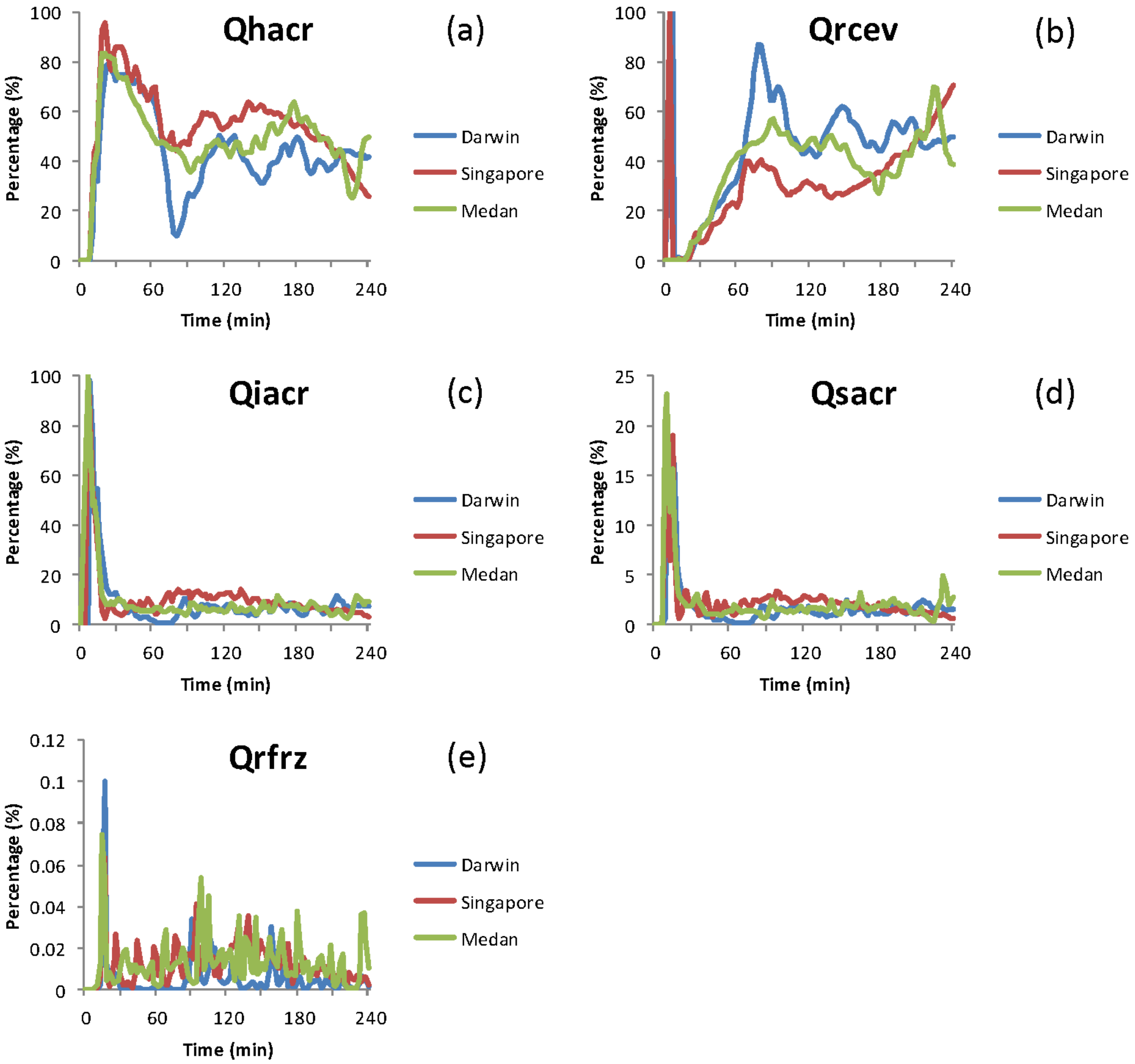

Figure 10. Superimposed time series in all three storm simulations for the rain sinks: (a) qhacr, (b) qrcev, (c) qiacr, (d) qsacr, (e) qrfrz. See the appendix for the microphysical meanings of the acronyms.

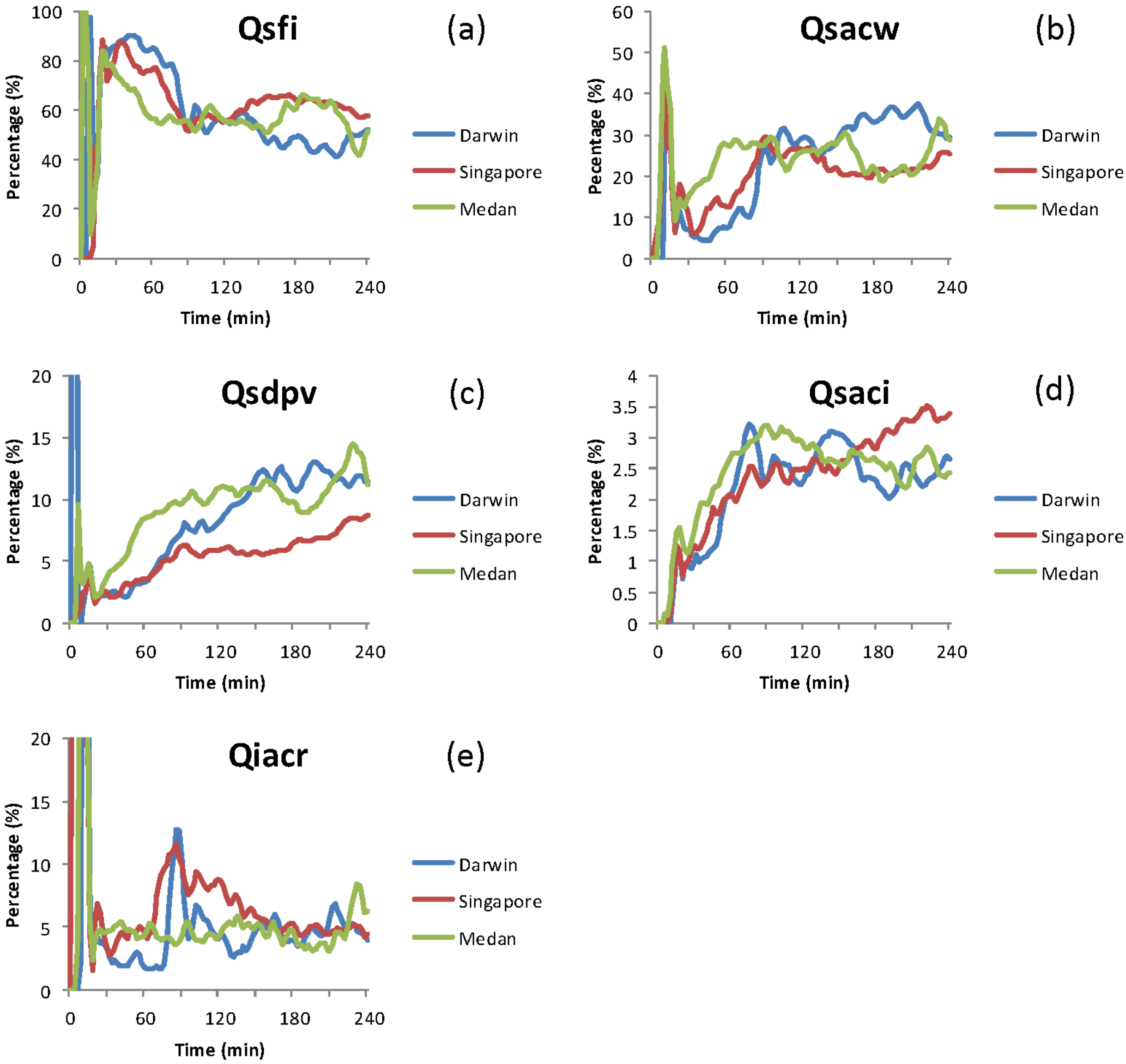

Figure 11. Superimposed time series in all three storm simulations for the snow sources: (a) qsfi, (b) qsacw, (c) qsdpv, (d) qsaci, (e) qiacr. See the appendix for the microphysical meanings of the acronyms.

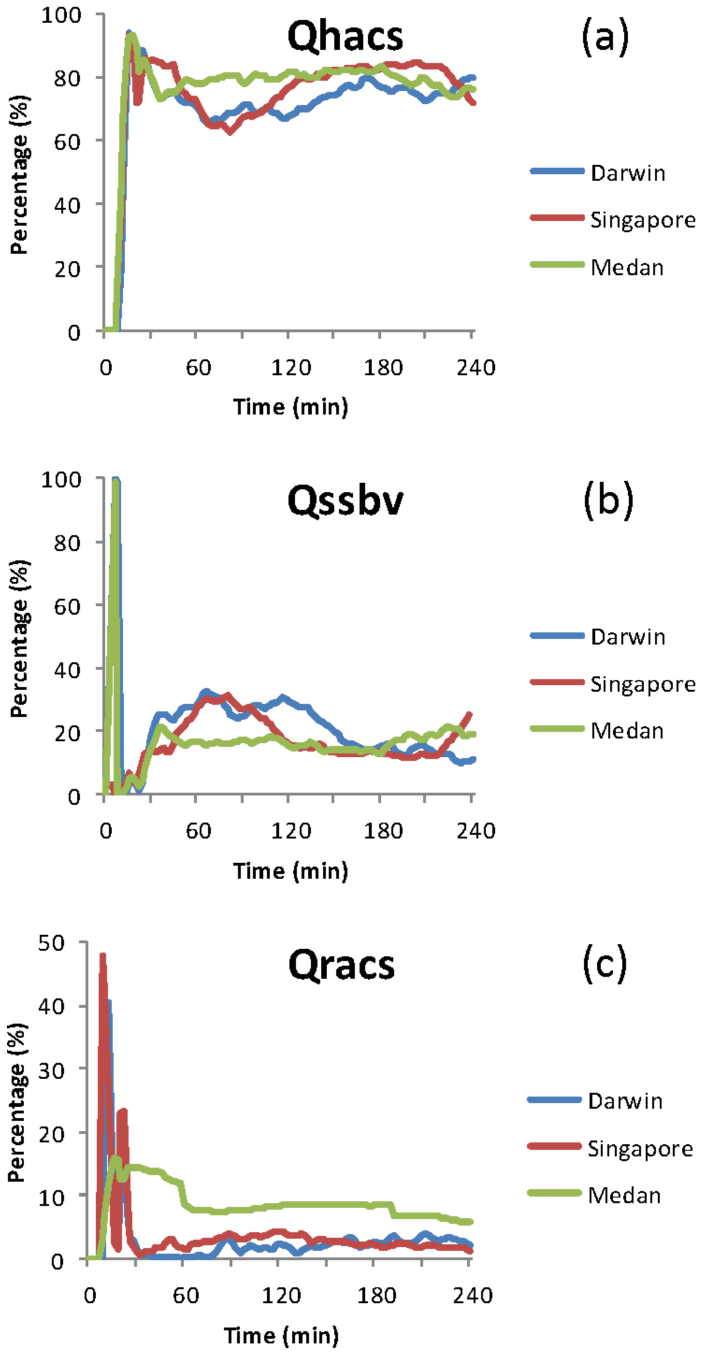

Figure 12. Superimposed time series in all three storm simulations for the snow sinks: (a) qhacs, (b) qssbv, (c) qracs. See the appendix for the microphysical meanings of the acronyms.

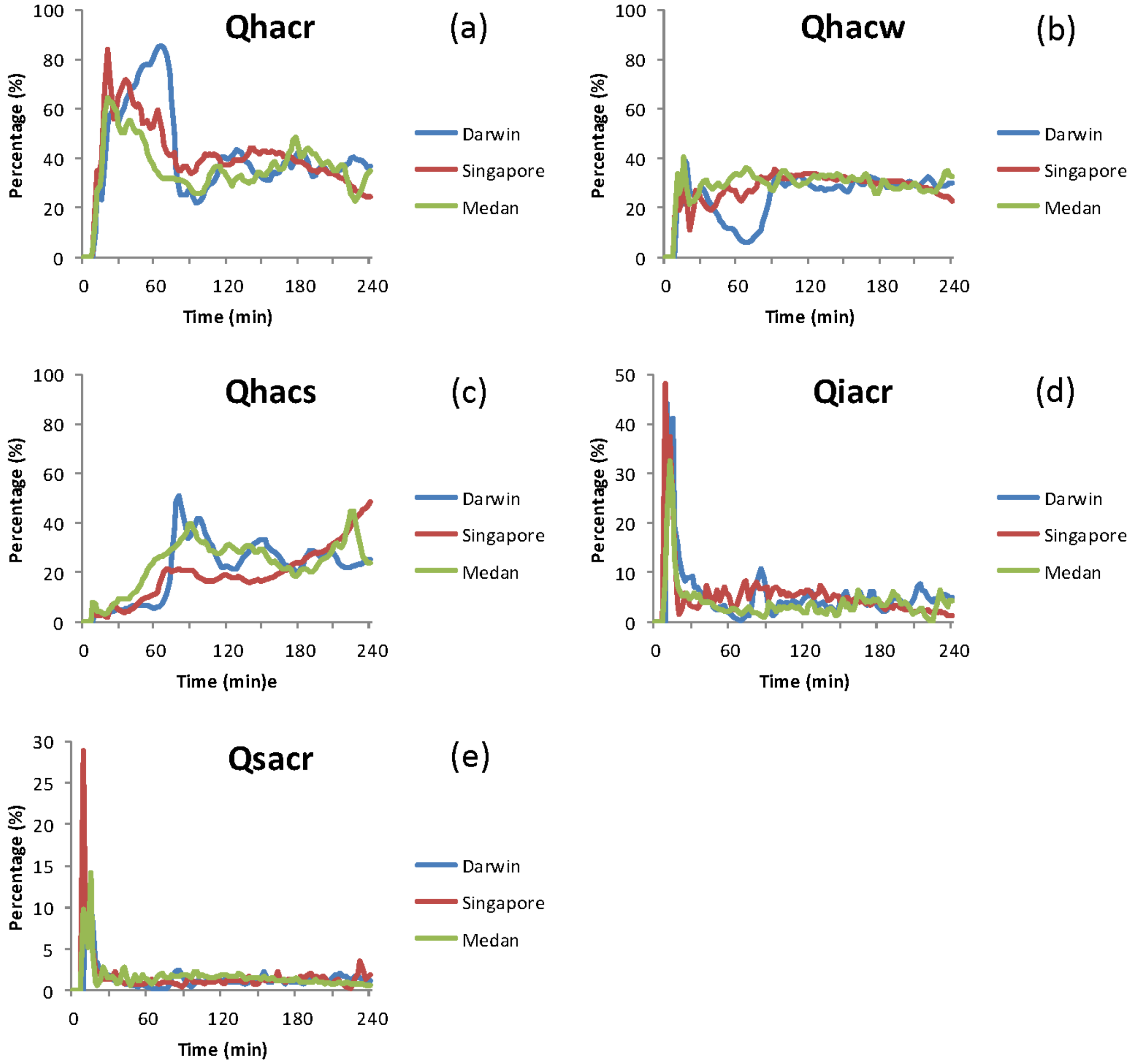

Figure 13. Superimposed time series in all three storm simulations for the hail/graupel sources: (a) qhacr, (b) qhacw, (c) qhacs, (d) qiacr, (e) qsacr. See the appendix for the microphysical meanings of the acronyms.

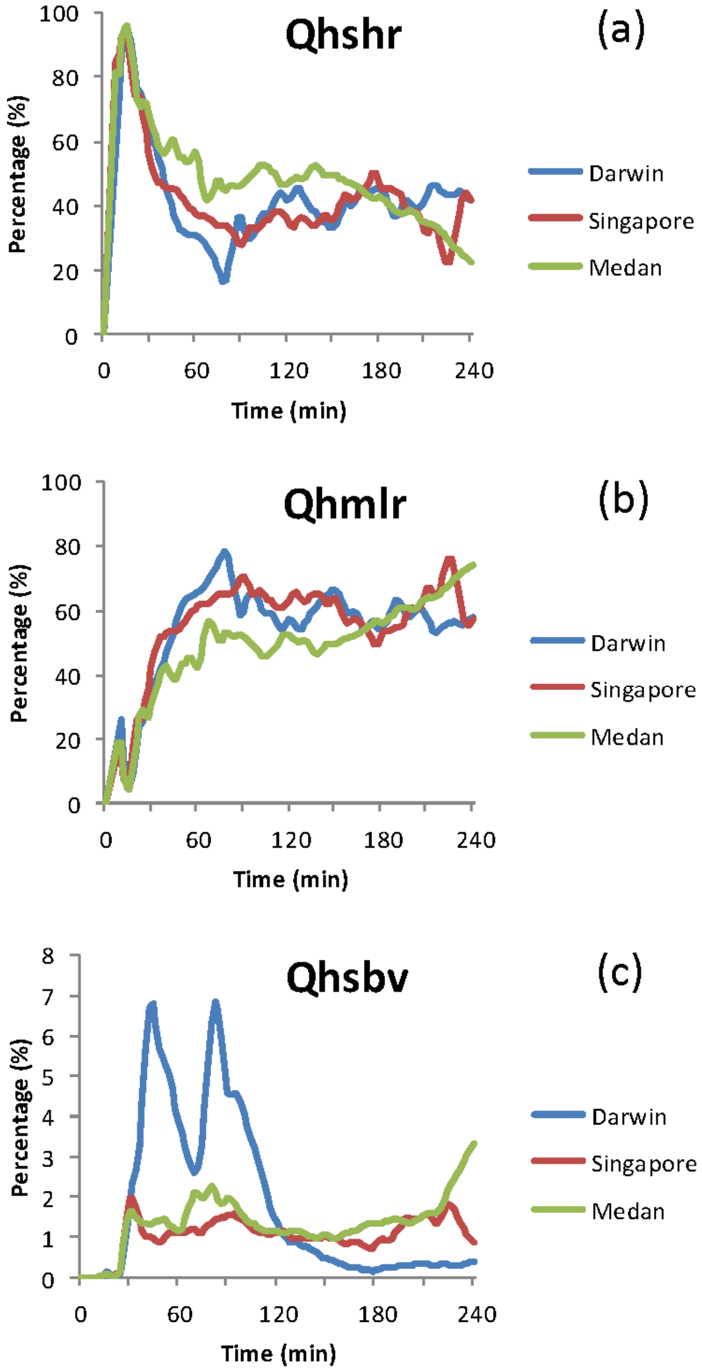

Figure 14. Superimposed time series in all three storm simulations for the hail/graupel sinks: (a) qhshr, (b) qhmlr, (c) qhsbv. See the appendix for the microphysical meanings of the acronyms.

The appendix. Definition of acronyms for microphysical processes

Acronym	Process
qhaci	Accretion of cloud ice by hail
qhacr	Accretion of rain by hail
qhacs	Accretion of snow aggregates by hail
qhacw	Accretion of cloud water by hail
qhcev	Condensation/Evaporation of vapor to/from wet hail
qhcns	Autoconversion of snow to hail
qhdpv	Vapor deposition to hail
qhmlr	Melting of hail to rain
qhsbv	Vapor sublimation from hail
qhshr	Rain water shed from hail
qhspait	Secondary production I of cloud ice from hail
qhspbit	Secondary production II of cloud ice from hail
qiacr	Accretion of rain by ice to form snow or hail
qiacw	Accretion of cloud water by cloud ice
qiint	Nucleation of pristine cloud ice
qimlw	Melting of cloud ice to cloud water
qivds	Vapor Deposition/Sublimation to/from cloud ice
qraci	Accretion of cloud ice by rain to form snow or hail
qracs	Accretion of snow by rain to form snow or hail
qracw	Accretion of cloud water by rain
qrcev	Evaporation of rain
qrcnw	Autoconversion of cloud water to rain
qrfrz	Probabilistic freezing of rain to form snow or hail
qsaci	Accretion of cloud ice by snow
qsacr	Accretion of rain by snow to form snow or hail
qsacw	Accretion of cloud water by snow
qscev	Condensation/Evaporation of vapor to/from wet snow
qscni	Autoconversion of cloud ice to snow
qsdpv	Vapor deposition to snow
qsfi	Bergeron process, transfer of cloud ice to snow
qsfw	Bergeron process, transfer of cloud water to snow
qsmlr	Melting of snow to rain
qssbv	Vapor sublimation from snow
qsspait	Secondary production I of cloud ice from snow
qsspbit	Secondary production II of cloud ice from snow
qvcnd	Condensation/Deposition to/on cloud water/cloud ice
qves	Evaporation/Sublimation of cloud water/cloud ice
qwfzi	Homogeneous freezing of cloud water to cloud ice